White Matter Microstructure Fingerprint of Cerebral Small Vessel Disease

Aurélie Bussy[1], Camille Cathala[4,5], Fábio Carneiro[1,2], Ferath Kherif[4], Antoine Lutti[4], Bogdan Draganski[1,3,4]

[1] Imaging Neuroscience of Ageing laboratory inAGE, Universitätsklinik für Neurologie, Inselspital Bern, University of Bern, Switzerland
[2] Graduate School for Health Sciences, University of Bern, Bern, Switzerland
[3] Institute for diagnostic and interventional neuroradiology, Inselspital Bern, University of Bern, Switzerland
[4] Laboratory for Research in Neuroimaging LREN, Centre for Research in Neurosciences, Department of Clinical Neurosciences, Lausanne University Hospital and University of Lausanne, Lausanne, Switzerland.
[5] Signal Processing Laboratory 5, Ecole Polytechnique Fédérale de Lausanne, Switzerland

ORCID
Aurélie Bussy https://orcid.org/0000-0001-6695-9941
Camille Cathala https://orcid.org/0009-0000-5755-9209
Fábio Carneiro https://orcid.org/0000-0001-7198-9520
Ferath Kherif https://orcid.org/0000-0001-5698-0413
Antoine Lutti https://orcid.org/0000-0003-3281-5477
Bogdan Draganski https://orcid.org/0000-0002-5159-5919

Correspondence to: Aurélie Bussy (aureliee.bussy@gmail.com) and Bogdan Draganski (bogdan.draganski@insel.ch)

Address: Rosenbühlgasse 25, 3010 Bern, Switzerland

Keywords: White matter hyperintensities, normal-appearing white matter, microstructural imaging, cardiovascular risk factors

Acknowledgments and funding:
B.D. is supported by the Swiss National Science Foundation (project grant no. 213595, 32003B_135679, 32003B_159780, 324730_192755 and CRSK-3_190185), InnoSuisse Flagship Swiss brAInHealth project, ERA_NET NEURON JTC2020: iSEE and JTC2023-ELSA: BrainTree projects. F.K. is funded by the PHASE IV AI/Horizon Europe grant, grant agreement ID: 1010953844:01 and Horizon 2020 (871643-MORPHEMIC). A.L. is supported by the Swiss National Science Foundation (Grant Nos. 320030_184784, CR00I5-235940). The Laboratory for Research in Neuroimaging (LREN) is very grateful to the Roger De Spoelberch and Partridge Foundations for their generous financial support. We wish to thank all BrainLaus participants for their participation in the study.

Competing interests
The authors declare no competing interests.

Abstract

There is much controversy about the spatial heterogeneity and microstructural characterisation of white matter hyperintensities (WMHs), the neuroimaging hallmark of cerebral small vessel disease. To address this knowledge gap, we analysed relaxometry and diffusion-weighted magnetic resonance imaging (MRI) together with cardiovascular risk data in a community-dwelling adult cohort (202 participants, mean age: 69.2 years, range: 53.3-85.4 years, 110 females). Following automated WMH detection, we compared MRI-derived metrics of tissue myelination, iron content, axonal density, and extracellular water, between WMH and normal-appearing white matter (NAWM). Principal component analysis demonstrated a pattern of demyelination, axonal loss, and extracellular fluid accumulation, particularly pronounced in periventricular regions. The layer-specific profiles of theWMHs revealed a centrifugal gradient of white matter vulnerability, with myelin loss and extracellular water accumulation, interpreted as oedema, at the core, and ongoing axonal reorganization and demyelination in the surrounding tissue. The obtained signatures of white matter pathology were intimately linked to the aging-related increase in cardiovascular risk. High blood pressure and impaired glucose regulation, together with reduced cholesterol and hemoglobin levels, emerged as key contributors. Our findings suggest that WMHs represent the radiologically visible endpoint of a more widespread white matter damage in cerebral small vessel disease. This underscores the pressing need for early detection and consequent treatment of cardiovascular risk factors.

1. Introduction

White matter hyperintensities (WMH) are radiological features commonly observed in conventional magnetic resonance images such as Fluid Attenuated Inversion Recovery (FLAIR), in older adults. They are considered a hallmark of cerebral small vessel diseases (SVD), most often reflecting vascular injury such as arteriolosclerosis or cerebral amyloid angiopathy (CAA). WMHs are frequent incidental findings and are associated with increased risk for gait impairment, stroke, and cognitive decline (de Leeuw et al. 2001; Sharma et al. 2024). Neuropathology studies indicate that WMHs reflect tissue damage due to demyelination, axonal loss, and gliosis (Grinberg and Thal 2010; Wardlaw, Smith, and Dichgans 2019), yet their biological mechanisms and temporal dynamics remain poorly defined. Although consistently associated with cardiovascular risk factors (CVR) and systemic inflammation (Wartolowska and Webb 2021; Lampe et al. 2019; Solé-Guardia et al. 2023; Schilling et al. 2014), the spatial progression and microstructural consequences of WMHs in relation to these systemic factors remain largely underinvestigated.

Emerging evidence challenges the traditional view of WHM as discrete lesions. Rather, they suggest that WMHs represent the macroscale imaging signature of a widespread white matter damage that also affects the surrounding normal-appearing white matter (NAWM) (Maniega et al. 2015). This broader pathological process appears to follow a centrifugal gradient of tissue damage extending outward from the core lesion, potentially reflecting secondary neuroinflammatory response, axonal degeneration, or impaired remyelination. To support this gradient model, studies have demonstrated that the area surrounding WMHs is characterised by changes in diffusion tensor metrics indicative of microstructural damage, defined as WMH penumbra (Maillard et al. 2014, 2011). At a different spatial scale, the WMHs and NAWM microstructure characteristics may vary depending on their proximity to the ventricles or cortex (Voorter et al. 2024), or along the antero-posterior brain axis (Habes et al. 2016; Veldsman et al. 2020; Piguet et al. 2009). This regional heterogeneity probably reflects differences in vascular areas and vulnerability to cardiovascular stressors, but the underlying mechanisms are still poorly understood.

Clinically, FLAIR imaging remains the standard for WMH detection and progression tracking (Hajnal et al. 1992). However, these images can be difficult to interpret, as a range of pathological processes, including edema, inflammation, and demyelination lead to the same signal abnormalities (Wardlaw, Smith, and Dichgans 2013). Quantitative MRI partly alleviates this limitation (Iordanishvili et al. 2019; Courtney et al. 2025). Relaxometry metrics provide information on tissue composition: magnetization transfer saturation (MTsat) and longitudinal relaxation rate (R1 = 1/T1) are sensitive to myelin content (Callaghan et al. 2014; Helms, Dathe, and Dechent 2008; Lutti et al. 2014), while the transverse relaxation rate (R2* = 1/T2*) primarily reflects iron accumulation but is also modulated by myelin (Fukunaga et al. 2010; Stüber et al. 2014; Oliveira et al. 2025). The fractional anisotropy (FA) index computed from diffusion MRI data reflects fiber coherence, mean diffusivity (MD) reflects overall water mobility, intracellular volume fraction (ICVF) captures axonal/neurite density, isotropic volume fraction (ISOVF) reflects extracellular free water,

and orientation dispersion (OD) indexes neurite geometry and angular variability (Parent et al. 2025).

Together, these complementary qMRI metrics provide a multiparametric characterization of brain tissue that goes beyond any single modality. While each parameter is sensitive to a specific biological substrate -such as myelin, iron, axonal density, or extracellular water-, their joint assessment enables a more holistic view of microstructural integrity. This integrative approach is often described as an *in vivo* histology framework (Weiskopf et al. 2021), as it allows researchers to infer cellular- and molecular-level features non-invasively, bridging the gap between conventional MRI contrasts and histopathological validation. Most prior work has shown that WMH are associated with demyelination or axonal loss, however they have focused on isolated brain regions or single imaging metric, limiting our understanding of how lesions and surrounding NAWM interact across the brain.

In this study, we leverage a comprehensive multicontrast MRI dataset from a cohort of older adults to investigate: first, the microstructural properties of WMH and NAWM across distinct white matter compartments. Second, using regional, multivariate, and layer-specific analyses, we characterize the pattern, extent, and spatial distribution of white matter pathology. Third, we further examine how cardiovascular risk factors and their treatment relate to both lesion burden and microstructural variations, aiming to disentangle shared and region-specific mechanisms of vulnerability. By integrating these dimensions, we provide detailed insights into the mechanisms through which specific cardiovascular risk factors and treatments impact microstructural health, informing strategies for targeted prevention of white matter degeneration in aging.

2. Methods

a. Participants

We analysed brain imaging data acquired in the BrainLaus project, a nested study of the epidemiological CoLaus|PsyCoLaus longitudinal cohort, focusing on investigations of cardiovascular risk factors and mental health (Firmann et al. 2008; Preisig et al. 2009). From the 423 participants with available FLAIR images, we excluded 60 individuals from further analysis due to bad image quality, and 161 due to missing cardiovascular data, resulting in a final sample of 202 participants (mean age: 69.2 years; range: 53.3-85.4 years; 110 females). Ethical approval was granted by the Ethics Commission of Canton de Vaud, and participants gave their informed consent prior to participation.

b. Cardiovascular risk factors

We included the following cardiovascular risk factors: <u>physiological measures:</u> systolic (SBP) and diastolic blood pressure (DBP) in mmHg as the average of the second and third out of three measurements; body mass index (BMI); bio-impedance, providing the percentage of fat mass; waist-to-hip ratio (WHR); <u>blood work-up</u>: HDL cholesterol, LDL cholesterol, total cholesterol, triglycerides, blood glucose, insulin, glycated hemoglobin (HbA1c),

high-sensitivity C-reactive protein (CRP), hemoglobin, thyroid-stimulating hormone (TSH), free thyroxine (FT4); lifestyle factors: alcohol consumption (units per week), caffeine intake (nr caffeinated drinks per day) and cigarette consumption (nr cigarette equivalents per day) (for details see Supplementary figure 1A). Outlier detection was performed separately for each risk factor by assigning NaN to values exceeding ±2.5 standard deviations from the mean. Significant cross-correlations between these variables are presented in the heatmap shown in Supplementary figure 1B.

The pharmacological treatment of cardiovascular factors was extracted via ATC codes. We classified medications by their main therapeutic use and counted them per treatment type according to the ATC hierarchical classification. Details of the ATC classification, including the number of medications per category with their mean and standard deviation, are provided in Supplementary methods and Table 1.

c. MRI acquisition

All MRI data were acquired from 02/2022 to 07/2024 on a 3T whole-body Siemens Magnetom Prisma system with a 64-channel radiofrequency (RF) receive head coil and a body coil for transmission. No major hardware or software update was conducted over the duration of the study.

i. FLAIR protocol

The FLAIR protocol included a repetition time (TR) of 5000 ms, an echo time (TE) of 389 ms and an inversion time (TI) of 1800 ms. Image resolution was 1 mm isotropic. To reduce the acquisition time, a GRAPPA acceleration factor of 2 was used along the phase-encoding direction and Partial Fourier factor of 7/8 was used along the slice direction.

ii. Relaxometry protocol

The relaxometry data was acquired using a custom-made 3D GRE pulse sequence (Weiskopf et al. 2013). Multi-echo images were acquired with T1- (TR/α = 18.7 ms/20°), PD- and MT-weighted contrasts (23.7 ms/6°) and TE between 2.2 ms and 19.7 ms (Draganski et al. 2011; Weiskopf et al. 2013). Additional acquisition parameters included: 1 mm isotropic resolution, a matrix size of 256 × 240 × 176, parallel imaging with a GRAPPA factor of 2 in the phase-encoding direction, 6/8 partial Fourier in the partition direction, non-selective RF excitation, a readout bandwidth (BW) of 425 Hz/pixel, and an RF spoiling phase increment of 50°, resulting in a total acquisition time of approximately 19 minutes. B1-mapping data was also acquired using the 3D EPI SE/STE method (Lutti et al. 2010, 2012) to correct for the effect of radio-frequency field inhomogeneities on the relaxometry data (Lutti et al. 2014).

iii. Diffusion-weighted protocol

For diffusion-weighted imaging (DWI), we used a 2D Echo-Planar Imaging (EPI) sequence with the following parameters: TR = 7400 ms, TE = 69 ms, parallel GRAPPA acceleration factor = 2, FOV = 192 × 212 mm², voxel size = 2 × 2 × 2 mm³, matrix size = 96 × 106, 70 axial slices, and 118 gradient directions (15 at b = 650 s/mm², 30 at b = 1000 s/mm², 60 at b = 2000 s/mm², and 13 at b = 0 interleaved throughout the acquisition) (Slater et al. 2019). Additionally, B0-field maps were acquired using a 2D double-echo FLASH sequence with a

slice thickness of 2 mm, TR = 1020 ms, TE1/TE2 = 10/12.46 ms, α = 90°, and readout BW = 260 Hz/pixel. These maps were used to correct for geometric distortions in the echo-planar imaging data.

d. MRI preprocessing

i. Quantitative maps estimation

Quantitative maps of magnetization transfer saturation (MTsat), the transverse relaxation rate (R2* = 1/T2*), the effective longitudinal relaxation rate (R1 = 1/T1), and the effective proton density (PD*) were computed from the raw MRI data using the VBQ toolbox (Draganski et al. 2011; Tabelow et al. 2019). The PD* maps were normalized assuming a mean value of 69% in white matter (Tofts 2003). However, because this normalization leads to a bias of the PD* values in white matter, PD* maps were excluded from further analyses. An example of the multi-parameter maps are presented along with the other modalities in Figure 1C.

ii. Diffusion MRI Processing

The DWI data underwent preprocessing using MRtrix3 (Tournier et al. 2019), which included denoising and removal of Gibbs ringing artifacts (Slater et al. 2019). Eddy current distortions and head movements were corrected with the FSL 5.0 EDDY tool (Andersson and Sotiropoulos 2016). Distortions of the EPI images were corrected using the FieldMap toolbox (Hutton et al. 2002) of SPM12 (Wellcome Trust Centre for Human Neuroimaging, https://www.fil.ion.ucl.ac.uk/spm) and the dedicated B0-field mapping data. The bias field was estimated from the mean b=0 images and corrected in all DWI datasets. Applying the tensor model, we obtained fractional anisotropy (FA) and mean diffusivity (MD) whole-brain maps. Using the neurite orientation dispersion and density imaging (NODDI) model and the multi-shell DWI data (H. Zhang et al. 2012), we calculated maps of intracellular volume fraction (ICVF), isotropic volume fraction (ISOVF) and orientation dispersion index (OD) using the AMICO toolbox (Daducci et al. 2015). MRI g-ratio maps, which represent the ratio between the inner and the outer diameter of the myelin sheath were created (Stikov et al. 2015; Slater et al. 2019). All obtained maps were aligned to the MTsat images using the rigid body registration tool of SPM12.

iii. FLAIR preprocessing

We used SPM12s “unified segmentation” for bias field correction of the FLAIR data (Penny et al. 2007) and CAT12 for denoising using a spatial adaptive non-local means denoising filter (Manjón et al. 2010). For rigid registration of FLAIR scans to MPM space was performed using FSL FLIRT (M. Jenkinson and Smith 2001; Mark Jenkinson et al. 2002).

iv. Quality control

We first performed a visual image quality control (QC) to all FLAIR images, MTsat, R1 and R2* maps as well as NODDI output maps. Images were discarded in case of motion artifacts, blurring, processing failures in any of the maps or in case of incidental findings such as meningiomas.

v. White matter hyperintensity assessment

A first assessment of the FLAIR images was performed visually to classify the lesions using the Fazekas descriptive scale (Fazekas et al. 1987). This scale categorizes WMH into periventricular (PVWM) and deep white matter regions (DWM), assigning a grade from 0 to 3 based on lesion size and confluence (0 indicating no lesion and 3 indicating extended lesions). In our study, scores from both regions were summed to create an overall lesion severity score ranging from 0 to 6 (figure 1A). Descriptions of our dataset classification in terms of lesion extent are given in figure 1B.

We then used an in-house deep learning algorithm for automated definition of WMHs on FLAIR images (Cathala et al. 2025). We applied this algorithm to FLAIR images co-registered to MTsat maps, yielding WMH and WM masks. From these outputs, we created a normal appearing white matter (NAWM) mask defined as the remaining WM voxels after exclusion of the WMHs. The WMH masks were subsequently dilated successively from 1 to 5 voxels, to ensure full spatial coverage of the transition from WMH to NAWM. Two concentric inner layers were generated within each WMH by eroding the lesion mask by 1 and 2 voxels to assess the uniformity of lesion characteristics.

For detailed characterisation of WMHs spatial distribution in the white matter, we defined the following partitions/compartments: i. binary ventricular mask - the sum of the left and right ventricular voxels from the FreeSurfer's Synthseg (Billot et al. 2023) ; ii. periventricular white matter (PVWM) mask - after dilating the ventricular mask by 8 voxels and subtracting the original ventricular mask ; iii. superficial white matter (SWM) mask after subtracting the original WM mask by the WM mask eroded by two voxels; iv. deep white matter (DWM) mask - after subtraction of the PVWM and SWM from the remaining WM.

For the spatial analysis across cerebral lobes, we used regions of interest derived from the probabilistic and maximum probability tissue labels provided by the "MICCAI 2012 Grand Challenge and Workshop on Multi-Atlas Labeling" and applied them to the MTsat maps (https://my.vanderbilt.edu/masi/about-us/resources-data/) (Yan et al. 2021). From these labels, we selected the cortical regions and grouped them anatomically into frontal, parietal, temporal, and occipital lobes. We assigned each white matter voxel to the nearest lobe by calculating its distance to the closest cortical voxel (Figure 1C).

vi. Parameter estimates extraction

The R1, MTsat, R2*, FA, MD, g-ratio, ISOVF, ICVF, OD regional averages were extracted in native MTsat space across the WMH, NAWM, in the PVWM, SWM, and DWM regions, within each layer masks (layers -1 to -2 and +1 to +5) or in each lobe or intersection of region and lobe.

e. Statistical analyses

i. Methodology

Our statistical analyses follow five complementary analyses, to address our main hypotheses. First, we characterized *"lobar and regional microstructural fingerprints"* to establish fundamental WMH-NAWM differences. We then investigated *"associations between WMH burden and microstructural signatures"* to understand volume-damage relationships. To identify dominant patterns, we examined *"regional white matter microstructure"* using principal component analysis. Next, we mapped *"layer-based microstructural profiles"* to characterize spatial gradients around lesions. Finally, we tested *"associations with cardiovascular risk and treatment"* to connect imaging findings to systemic health factors using multivariate methods.

ii. Technical implementation

Layer masks creation, metric sampling, and statistical analyses were performed in Python 3.8.19 using Jupyter Notebook. Analyses were conducted on z-scored quantitative MRI metrics, calculated across participants for each region and tissue type (WMH and NAWM). Prior to statistical testing, outlier detection was applied on a per-metric, per-region basis: values exceeding ±2.5 standard deviations from the regional mean were replaced with NaN and excluded from subsequent analyses.

To quantify within-subject differences between WMH and NAWM, we computed paired Cohen's d (dz; WMH-NAWM divided by the SD of within-subject differences) for each metric and region, providing a standardized effect size across metrics. WMH-NAWM contrasts were tested with the Wilcoxon signed-rank test (paired), with Benjamini-Hochberg FDR correction across metric*region tests. Regional and lobar differences were estimated using the Kruskal-Wallis test. Linear relationships between MRI metrics and regional WMH volumes were tested using ordinary least squares (OLS) regression.

To identify predominant patterns of microstructural variation across participants, metrics, and regions, we performed principal component analysis (PCA) using Scikit-learn (v1.3.2). The input matrix included one column per metric, region, and tissue type i.e., for each region and each metric, one column was created for WMH and one for NAWM. Metric values were averaged per participant and z-scored across participants and regions.

Layer-wise analyses were conducted to capture the spatial gradient of microstructural changes from the WMH core to surrounding white matter. For each metric, third-order polynomial fits were applied to model changes across layers, and the derivatives between adjacent layers were calculated. These derivatives were normalized within each segment such that the maximum absolute value equaled ±1, allowing direct comparison of the relative rate of change across metrics and layers.

To test for multivariate associations between white matter microstructure and CVR or medication, we used partial least squares (PLS) analysis (https://github.com/rmarkello/pyls; (McIntosh and Lobaugh 2004)). The brain input matrix included one column per region × metric × tissue type (WMH or NAWM), enabling separation of the associations of CVR/medication with NAWM and WMH microstructure. The CVR and medication input

matrices included one column per risk factor or medication category. All variables were z-scored prior to PLS. This approach decomposes the brain and CVR matrices into latent variables (LVs) that capture shared variance across both domains. The significance of each LV was tested via permutation, and variable contributions were assessed using bootstrap resampling, following established protocols (McIntosh and Lobaugh 2004; Zeighami et al. 2019; Patel et al. 2020; Bussy et al. 2021, 2023, 2025).

All p-values were corrected for multiple comparisons using the Benjamini-Hochberg false discovery rate (FDR) method, with significance threshold set at $p < 0.05$.

f. Data availability statement

Data from BrainLaus dataset is not publicly available but can be requested upon reasonable and formal request (https://www.colaus-psycolaus.ch/professionals/how-to-collaborate). All our data extraction, analysis code, results and figures can be found on GitHub (https://github.com/AurelieBussy/WMH_analyses).

A

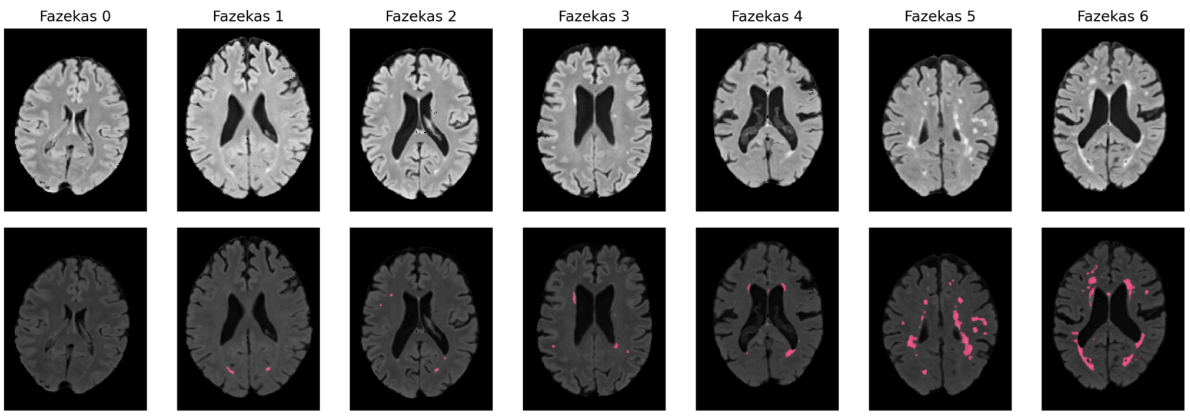

B

Fazekas category	0	1	2	3	4	5	6
n	9	35	53	38	30	21	16
Mean age	63,7	66,2	66,7	71,1	71,8	71,3	75,3
% males	55,6	62,9	49,1	31,6	46,7	38,1	31,2

C

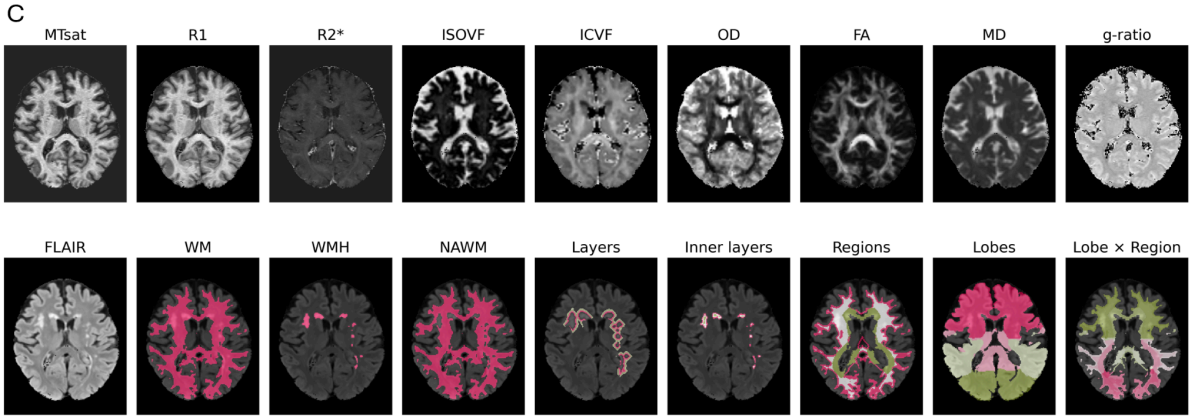

Figure 1: Representative subject data and white matter segmentation framework. A. Examples of brains classified from Fazekas grade 0 (no WMH) to grade 6 (large WMH in deep and periventricular white matter). **B.** Summary table showing the distribution of our 203 participants across Fazekas grades with corresponding age and sex. **C.** Illustrative maps from one participant (82-year-old female) showing quantitative MRI metrics, FLAIR, and tissue masks. The maps include myelin- and iron-sensitive metrics (MTsat, R1, R2*), axon-sensitive metrics (ICVF, OD, FA), and fluid/composite metrics (ISOVF, MD, g-ratio), alongside masks for WM, WMH, NAWM, outer and inner layers, WM regions (SWM, DWM, PVWM), lobes (frontal, parietal, temporal, occipital), and individual WMH lesions. ***Abbreviations:*** *magnetization transfer saturation (MTsat), longitudinal relaxation (R1), transverse relaxation (R2), intracellular volume fraction (ICVF), orientation dispersion (OD), fractional anisotropy (FA); isotropic volume fraction (ISOVF), mean diffusivity (MD), white matter (WM), white matter hyperintensities (WMH), normal-appearing white matter (NAWM), superficial white matter (SWM), deep white matter (DWM), periventricular white matter (PVWM).*

3. Results

a. Lobar and regional microstructural fingerprints of WMH versus NAWM

We observed MRI parameter differences between WMH and NAWM across almost all metrics and regions (Figure 2AB). Across regions, we found lower values of MTsat (d = -3.47), R1 (d = -3.53), R2* (d = -3.02), ICVF (d = -3.08), FA (d = -1.71), and OD (d = -1.17); in WMH compared to NAWM. We found higher values of MD (d = 3.19) and ISOVF (d = 2.05) in WMH compared to NAWM, and small differences of the MRI g-ratio (d = -0.13) This constellation of changes is consistent with demyelination, reduced axonal density, and increased extracellular water, with relatively minor alterations in fiber orientation and myelin-to-axon size ratio. We also observed regional heterogeneity in directionality for certain metrics such as for OD, FA, and g-ratio. For example, OD was higher in WMH compared to NAWM in PVWM frontal regions (d = 1.54) but lower in PVWM occipital regions (d = –2.41), suggesting that lesion-related changes in neurite orientation and fiber architecture are not uniform, but instead vary according to regional white matter organization.

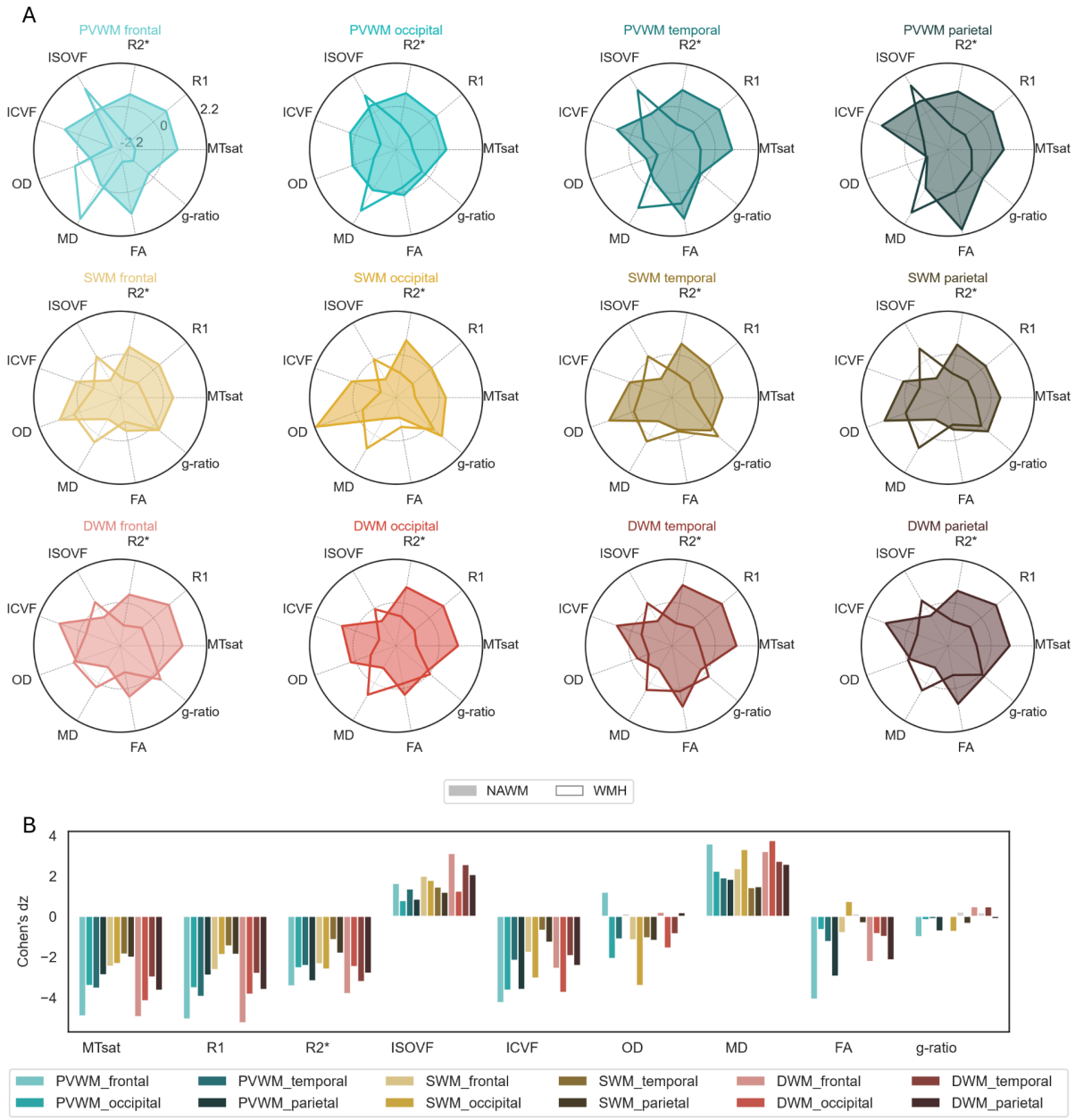

Figure 2. Regional comparison of white matter MRI microstructure metric between WMH and NAWM. A. Mean values of MTsat, R1, R2*, ISOVF, ICVF, OD, MD, FA and g-ratio were computed for WMH and NAWM across lobar (frontal, occipital, temporal, parietal) and regional white matter subdivisions (SWM, DWM, PVWM). After z-scoring per metric across WMH and NAWM in all regions, radar plots illustrate regional microstructural profiles for each tissue type. **B.** Group differences (WMH vs NAWM) were quantified using Cohen's *dz* and summarized in a barplot, highlighting effect sizes across metrics and regions. *Coloured bars indicate regions with significant group differences after FDR correction (p<0.05); non-significant effects are shown in grey (OD PVWM parietal, FA SWM temporal, g-ratio SWM frontal and DWM occipital).* ***Abbreviations:*** *white matter hyperintensities (WMH), normal-appearing white matter (NAWM), magnetization transfer saturation (MTsat), longitudinal relaxation (R1), transverse relaxation (R2*), isotropic volume fraction (ISOVF), intracellular volume fraction (ICVF), orientation dispersion (OD), fractional anisotropy (FA), mean diffusivity (MD), superficial white matter (SWM), deep white matter (DWM),*

periventricular white matter (PVWM).

b. Associations between WMH burden and regional microstructural signature in NAWM and WMH

The burden of WMH, expressed by the logarithmic WMH volume per region and participant, showed marked regional differences (Kruskal–Wallis H = 497.87, $p < 0.001$; Figure 3A). WMH burden was highest in the frontal PVWM (mean log volume ± SD: 6.04 ± 2.15) and lowest in SWM and parietal/temporal regions (e.g., SWM parietal vs PVWM frontal, p = 3.35e-29). To contextualize these differences, we examined the total volume of NAWM across WM partitions (log-transformed; Kruskal–Wallis H = 2071.17, $p < 0.001$). As expected, NAWM volumes varied substantially by partition due to anatomical definitions, with SWM regions showing the largest volumes (frontal SWM: 11.32 ± 0.11) and occipital PVWM the smallest (8.64 ± 0.54; Figure 3B). Importantly, the volume fraction of WMHs in each white matter region was highest in the PVWM (5.21%, Figure 3C), highlighting the highest vulnerability of PVWM regions.

To assess how the lesion burden relates to tissue microstructure, we examined associations between regional WMH volume and the quantitative MRI metrics, measured in WMH and NAWM (Figure 3D). Greater WMH volume was associated with higher MD (+0.14), and lower R2* (-0.43), ICVF (-0.24), OD (-0.19), and g-ratio (-0.22). Importantly, greater WMH burden was also accompanied by more pronounced alterations in the surrounding NAWM, with lower MTsat (-0.34), R1 (-0.33), R2* (-0.26), ICVF (-0.36), FA (-0.29), and higher ISOVF (+0.33) and MD (+0.43). We further tested these associations at the regional and lobar levels (Figures 3F-G). The strongest effects were observed in NAWM PVWM regions, where MD showed the largest positive association ($\beta = +1.23$) and OD the largest negative association in the PVWM frontal ($\beta = -1.53$). In contrast, SWM occipital and parietal regions showed no significant associations across metrics ($p > 0.05$).

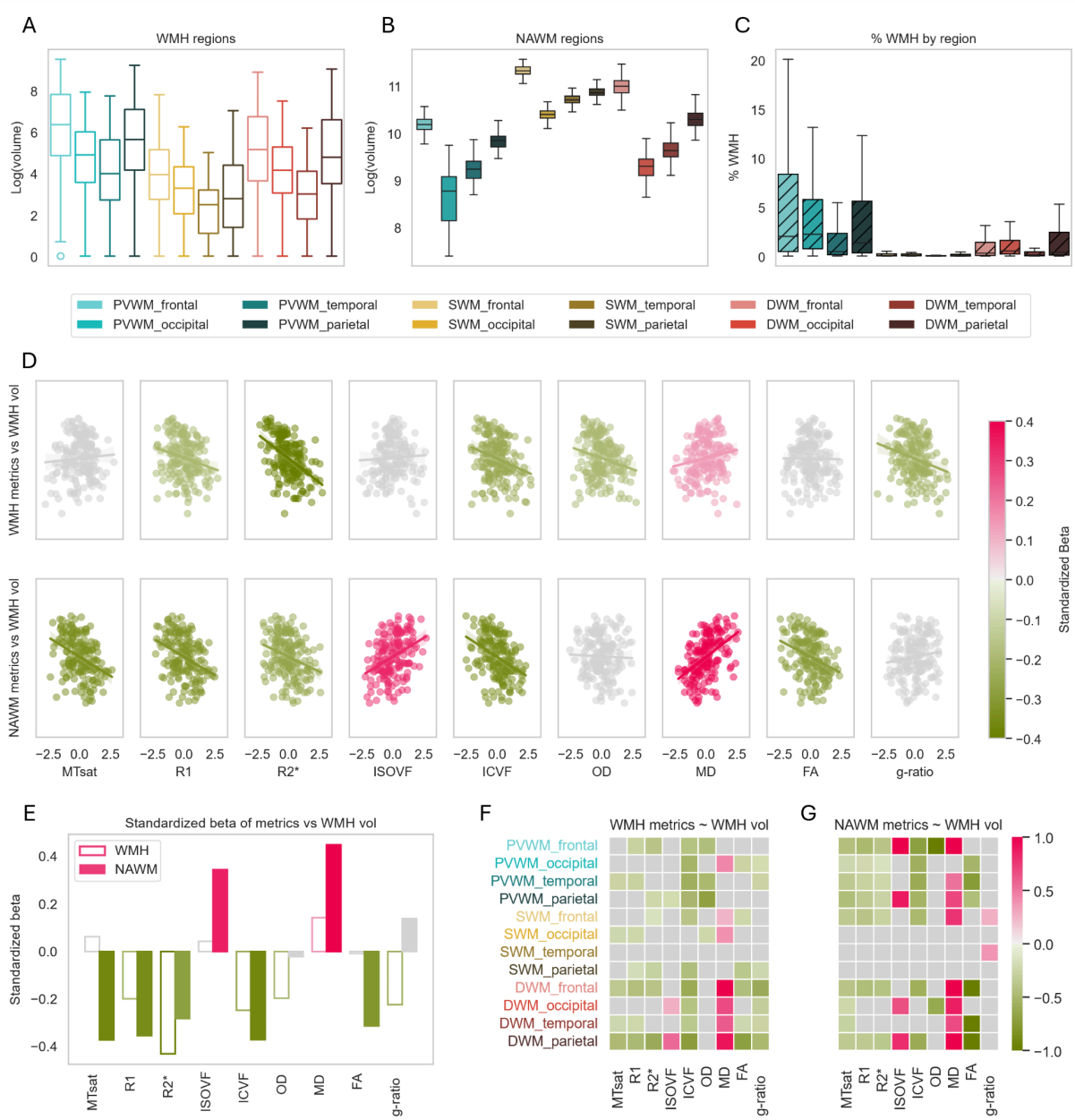

Figure 3. Regional distributions and associations of WMH and NAWM microstructure. **A.** Log-transformed volumes of WMH masks across the same regions. **B.** Log-transformed volumes of NAWM masks across lobar and regional white matter subdivisions. **C.** Proportion of WMH volume relative to total white matter volume per region. **D.** Linear relationships between regional WMH volume and microstructural metrics. **E.** Standardized beta coefficients summarizing the strength and direction of these associations for both WMH and NAWM. **F.** Heatmap of standardized beta values for WMH microstructure in relation to log WMH volume, highlighting region-dependent effects. **G.** Heatmap of standardized beta values for NAWM microstructure in relation to log WMH volume, also showing region-specific variation. *Coloured bars and plots indicate statistically significant associations after FDR correction ($p < 0.05$); non-significant results are shown in grey.* ***Abbreviations:*** *white matter hyperintensities (WMH), normal-appearing white matter (NAWM), magnetization transfer saturation (MTsat), longitudinal relaxation (R1), transverse*

relaxation (R2), isotropic volume fraction (ISOVF), intracellular volume fraction (ICVF), orientation dispersion (OD), fractional anisotropy (FA), mean diffusivity (MD), superficial white matter (SWM), deep white matter (DWM), periventricular white matter (PVWM).*

c. Regional white matter microstructure in WMH and NAWM

The regional microstructural PCA analysis of the qMRI metrics in the WMH and NAWM identified two main components: PC1, explaining 57.1% of the variance (p = 0.0001 after 10,000 permutations), and PC2, explaining 22.8% (p = 0.0001). PC1 reflected a pattern of low MTsat, R1, R2*, ICVF, and FA, combined with high ISOVF and MD, with minimal contributions from g-ratio and OD (Figure 4B). This profile showed the same directionality as the Cohen's d contrasts between WMH and NAWM in Figure 2B, consistent with widespread demyelination, iron loss, reduced axonal density, and increased extracellular water. PC2, in contrast, represented low ISOVF, FA, and MD alongside high OD and g-ratio (Figure 4C), suggestive of microstructural reorganization driven by altered neurite orientation and relative changes in axonal packing, rather than extracellular water accumulation. Notably, relaxometry metrics (MTsat, R1, R2*) contributed minimally to PC2, indicating that this axis of variation is largely independent of myelin- and iron-related processes, and instead captures differences in white matter geometry and fiber organization.

The projection of regional samples in PC space revealed distinct qMRI signatures for WMH and NAWM across regions (Figure 4D). PC1 primarily captured the contrast between WMH and NAWM, with WMH showing higher scores (mean = 2.41) than NAWM (–1.64; Mann–Whitney U = 3,252,654, $p < 0.0001$), reflecting widespread tissue degeneration. The greatest NAWM-WMH divergence along PC1 was observed in frontal PVWM (Euclidean distance = 5.54). This is also the region that shows the strongest associations between WMH volume and microstructural alterations in NAWM (Fig. 3G), indicating that frontal PVWM shows the largest microstructural tissue damage as a result of vascular lesions. In contrast, the smallest divergence NAWM-WMH in the temporal SWM (distance = 3.02) points to relatively preserved microstructural tissue properties in spite of the lesions.

By contrast, PC2 did not differentiate WMH from NAWM (U = 1,648,043, $p = 0.75$), but instead separated white matter regions (Kruskal–Wallis H = 2104.38, $p < 0.0001$), with higher values in SWM (1.47) than DWM (–0.07) or PVWM (–1.14; Fig. 4E). Along PC2, the largest divergence occurred in occipital SWM regions (distance = 2.11; Figures 4G–H), pointing to architectural differences in tissue organisation that are not directly lesion-driven but instead reflect inherent compartmental specialisation of white matter.

In supplementary analyses, we examined the relationship between WMH and NAWM microstructure using PC1 scores (Supplementary Figure 2). Across most regions, NAWM and WMH PC1 values were positively associated, and both increased with greater WMH volume, indicating that microstructural abnormalities in NAWM parallel those within lesions and scale with lesion burden. This suggests that NAWM alterations emerge in concert with lesion development, extending the impact of WMH beyond their visible boundaries.

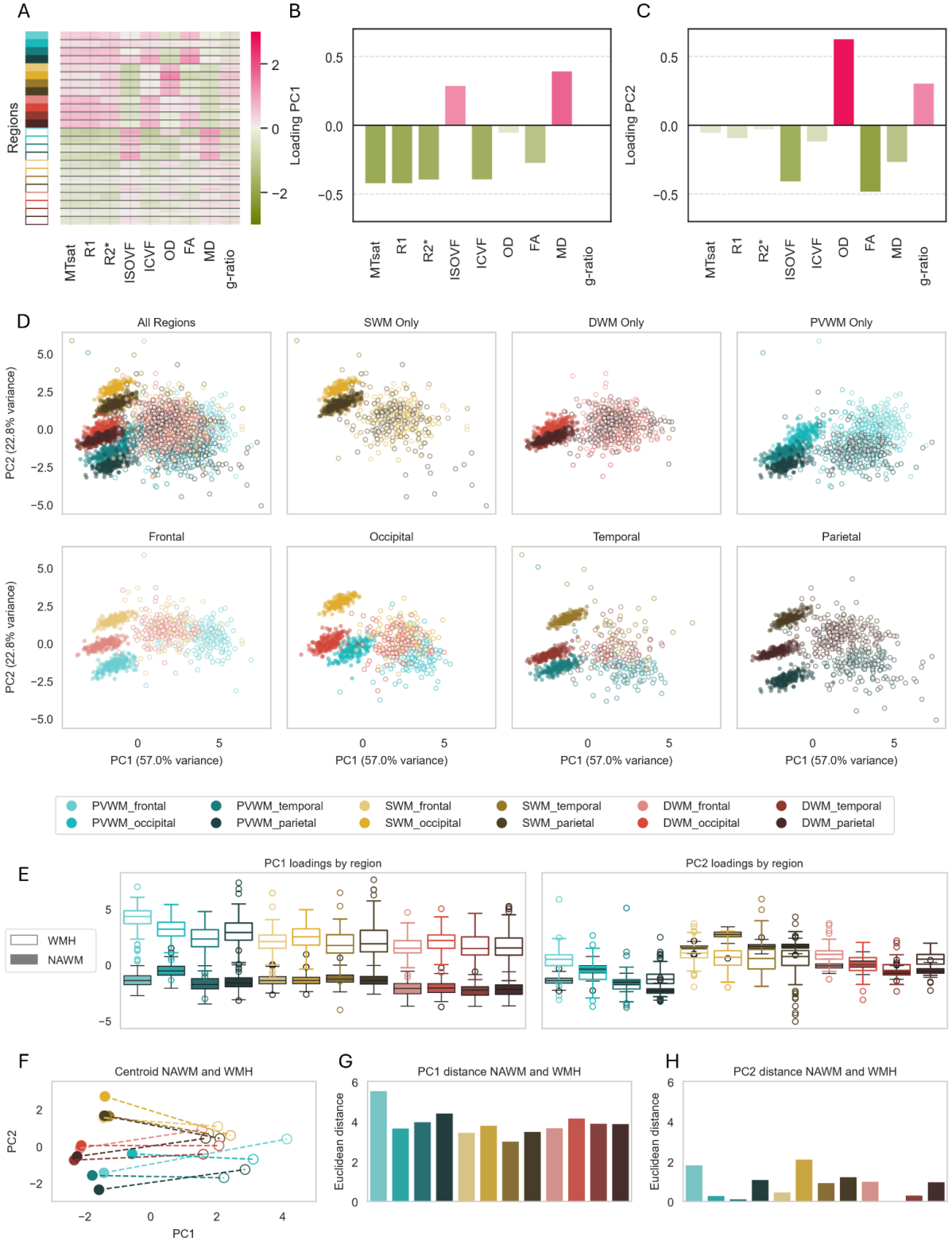

Figure 4. Principal component analysis of regional white matter microstructure in WMH and NAWM. We performed PCA on region-wise microstructural metrics across participants, using one NAWM measurement per region per individual, and multiple WMH regions per individual depending on the distribution of lesions. **A.** Heatmap of the standardized input matrix (regions × metrics) used for PCA. **B-C.** Barplots showing the

contribution (loadings) of each metric to PC1 (B) and PC2 (C). **D.** Projection of all regional WMH and NAWM samples onto the PC1-PC2 space. **E.** Boxplots showing the distribution of PC1 and PC2 scores across white matter regions for WMH and NAWM. **F.** Regional centroids in PC space summarizing the average WMH (empty dots) and NAWM (solid dots) profile per region. **G-H.** Barplots showing the Euclidean distance between paired WMH and NAWM centroids along PC1 (G) and PC2 (H), quantifying microstructural divergence across regions. ***Abbreviations:*** *white matter hyperintensities (WMH), normal-appearing white matter (NAWM), magnetization transfer saturation (MTsat), longitudinal relaxation (R1), transverse relaxation (R2*), isotropic volume fraction (ISOVF), intracellular volume fraction (ICVF), orientation dispersion (OD), fractional anisotropy (FA), mean diffusivity (MD), superficial white matter (SWM), deep white matter (DWM), periventricular white matter (PVWM), principal component (PC).*

d. Layer-based microstructural WMH profiles

We examined the spatial profile of microstructural differences from the WMH center outwards using a layer-centred analysis. In figure 5A, for each metric, we modelled the non-linear relationship between distance from the WMH center and microstructural values (lesion core, inner layers -2, -1, outer layers 1-5, and NAWM). By testing the difference between the layers vs the center per metric, we found differences across layers for all metrics (FDR-corrected $p < 0.01$ for all layers in all metrics except for ISOVF layer -2 vs center). Myelin- and axon-sensitive metrics (MTsat, R1, R2*, ICVF, FA) increased progressively from the WMH center toward NAWM, while markers of extracellular water content (MD, ISOVF) decreased along the same gradient. Most metrics reached their highest or lowest values either at the lesion center or in distant NAWM. However, some metrics peaked at intermediate distances from the lesion core (i.e. FA, R1), indicating that microstructural changes may not follow a simple linear gradient but reflect more complex spatial dynamics.

Figure 5B shows that the steepest changes in myelin and iron sensitive metrics (MTsat, R1, R2*) take place near the lesion core, particularly between the center and up to the second outer layer. The magnitude of change progressively decreases with increasing distance from the center. Axon-related metrics showed a different pattern: ICVFs differences were largest in the lesion center peaking between segments 1 and 3, before decreasing towards the outer layers. FA displays moderately high differences near the center, with a decrease beyond outer layer 2. OD shows minimal change in the central segments but demonstrates increasing spatial gradients in the outer layers beyond layer 1. For fluid-sensitive metrics, MD and ISOVF exhibit lower variation near the center, with increasing gradients in more peripheral segments, MD peaking between segments 2 and 4, and ISOVF peaking between segments 4 and 5. The g-ratio shows negligible change up to segment 1/2, with only modest increases in the outermost layers.

Figure 5C shows the standardized beta values of the association between age and each metric across layers, with colored dots indicating FDR-corrected significance ($p<0.05$). For myelin-sensitive metrics (MTsat, R1, R2*), beta values are near zero in central regions, with no significant age effects observed. R2* shows significant negative associations with age

starting from layer 1 and across all more peripheral layers. MTsat and R1 similarly show significant negative age associations beginning at layer 3 and extending outward. Among axon-sensitive metrics, ICVF and FA exhibit significant positive age-related effects in layers 1 and 2, shifting to significant negative associations in the outermost WM region. OD shows a significant negative association with age only at layer 1. For fluid-sensitive and composite metrics, ISOVF displays significant positive associations with age in the lesion center, layers -2 and -1, and in the WM region, though the effect is stronger centrally. MD shows no significant age effects except for a positive association in the WM region. The g-ratio demonstrates significant positive associations with age beginning at layer 2 and extending through the outer layers up to the WM region.

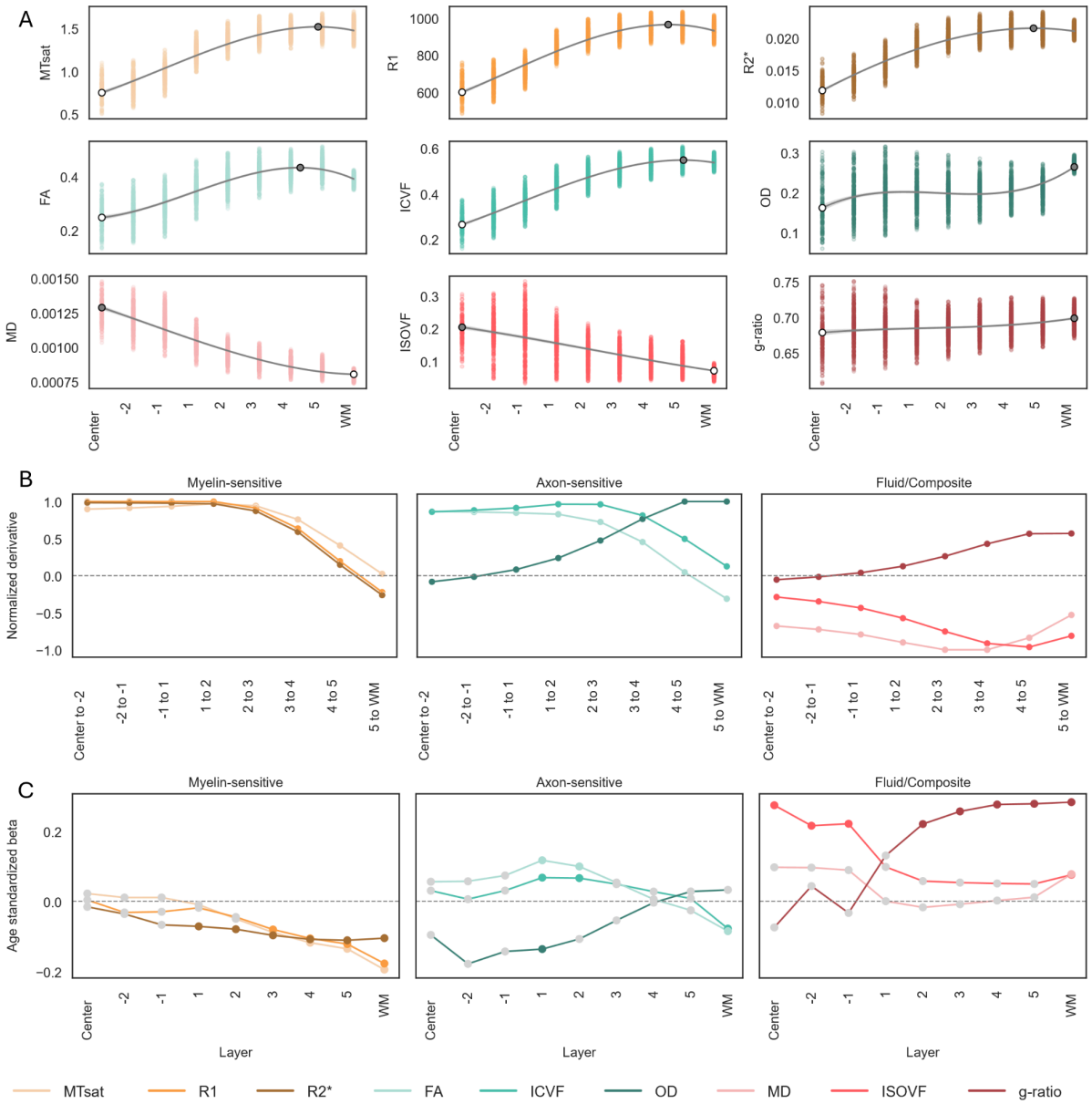

Figure 5. Layer-wise microstructural changes in the WMH penumbra. A. Scatterplots

showing layer-wise microstructural profiles across metrics, modeled using third-order polynomial fits. Layers span from the WMH center, through inner layers (-2, -1), to perilesional layers (1-5) and the rest of normal-appearing white matter (WM). White and grey dots indicate the layers at which the minimum and maximum metric values were observed, respectively. **B.** Normalized derivative of each metric's polynomial fit across layer segments. This represents the relative positive or negative rate of differences between adjacent layers, normalized within each segment for comparability. Metrics are grouped into myelin-sensitive (MTsat, R1, R2*), axon-sensitive (FA, ICVF, OD), and fluid/composite (MD, ISOVF, g-ratio) categories. Higher absolute derivative values reflect steeper spatial gradients, indicating more abrupt microstructural changes between adjacent layers. **C.** Standardized age β-coefficients (from ordinary least square regression models) showing the association between age and each metric within each layer. Lines connect the standardized betas across layers, while individual points are color-coded by metric and indicate statistical significance after FDR correction (colored if $p<0.05$, gray otherwise). This highlights how age-related microstructural alterations are spatially distributed across lesion layers, with distinct patterns depending on metric type and tissue property. ***Abbreviations:*** *magnetization transfer saturation (MTsat), longitudinal relaxation (R1), transverse relaxation (R2*), isotropic volume fraction (ISOVF), intracellular volume fraction (ICVF), orientation dispersion (OD), fractional anisotropy (FA), mean diffusivity (MD).*

e. Associations between white matter microstructure, cardiovascular risk, and treatment

We used PLS to investigate the relationship between white matter microstructure, CVR and pharmacological treatment. For the first analysis, we found a LV1 that explained 62.5% of the variance in the brain/CVR relationship ($p<0.001$, permutation test). LV1 demonstrated a microstructural signature primarily driven by NAWM, with lower R1, R2*, ICVF, FA, and MTsat alongside higher MD, ISOVF, and g-ratio. WMH metrics contributed less strongly, with lower WMH R1 and OD and higher WMH MD and ISOVF (Figure 6A). This profile is consistent with demyelination, axonal loss, and increased extracellular water, and was associated with higher age, SBP and HbA1c, as well as lower LDL, total cholesterol and reduced hemoglobin (Figure 6B).

In a second analysis linking brain and pharmacological treatments, we identified a significant LV1 explaining 45.9% of the variance ($p < 0.001$, permutation test). Again, the association was primarily driven by NAWM microstructure, showing a similar profile of myelin- and axon-related degeneration together with extracellular pathology, and was linked to greater use of antihypertensives and antiplatelet/anticoagulant medications, and reduced intake of respiratory treatments.

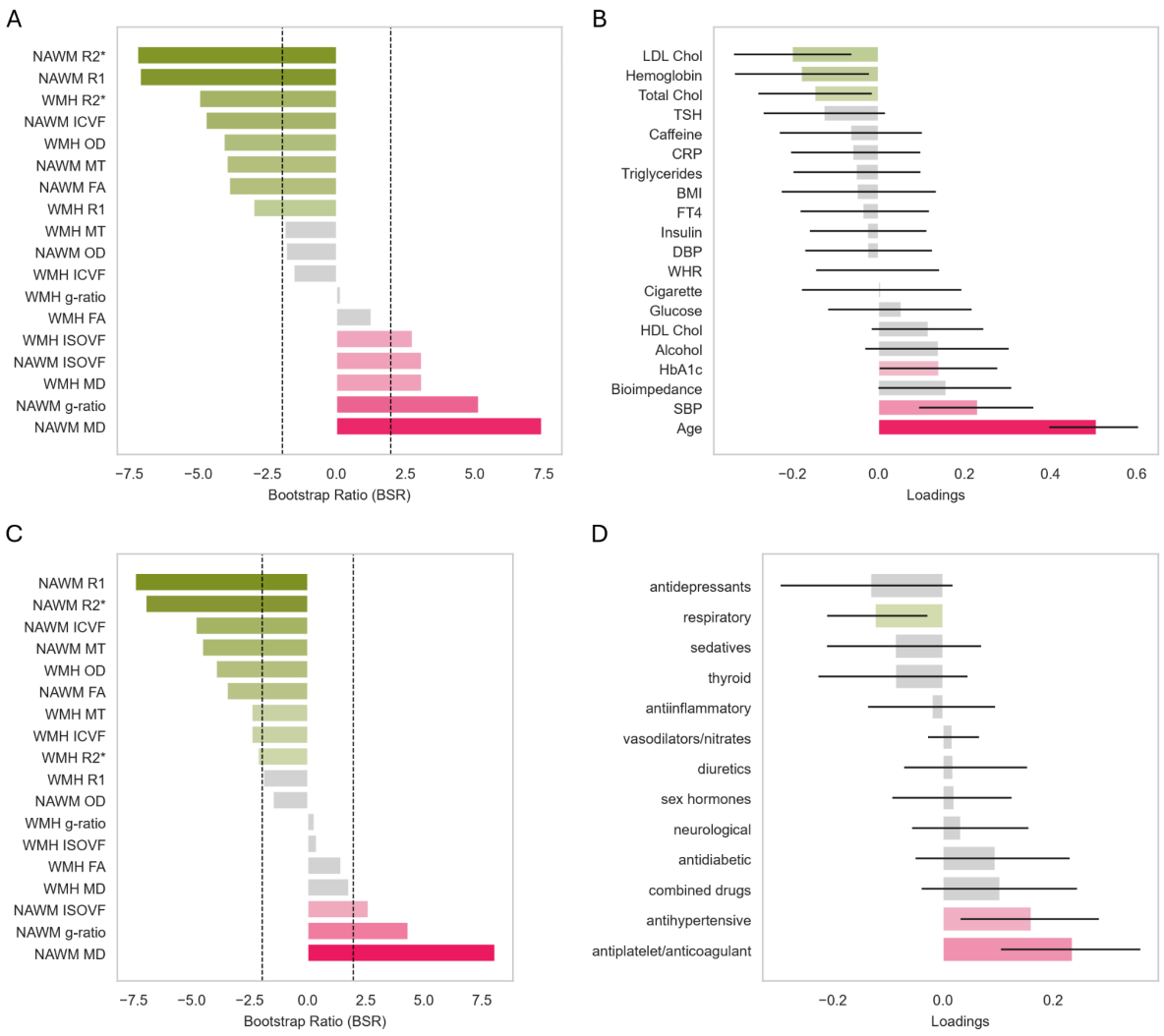

Figure 6. Partial least squares (PLS) analysis linking regional white matter microstructure to cardiovascular and medication-related variables. A. Bootstrap ratio (BSR) plot showing the contribution of MRI metrics to the first PLS component explaining 62.5% of the variance. Lower NAWM R1, R2*, ICVF, FA, and MTsat, and higher NAWM MD, ISOVF, and g-ratio, contribute most strongly. WMH R1 and OD show negative loadings, while WMH MD and ISOVF load positively. *Significant contributors (|BSR| > 1.96) are colored; non-significant in light gray.* **B.** Loadings for cardiovascular and medication variables on the first PLS component. *Significant variables (95% CI not crossing zero) are colored; others in light gray.* This pattern associates lower myelin and axon integrity and higher fluid-related metrics with increased age, systolic blood pressure (SBP), glycated hemoglobin (HbA1c), and with lower total cholesterol, hemoglobin, and LDL cholesterol. **C.** BSR plot of MRI metrics for the first PLS component linking microstructure to medication exposures, revealing a similar microstructural signature than in A and explaining 45.9% of the variance. **D.** Loadings for treatment variables showing associations with higher use of antihypertensives, antiplatelets/anticoagulants, and diuretics, and reduced use of respiratory treatments. ***Abbreviations:*** *white matter hyperintensities (WMH), normal-appearing white matter (NAWM), magnetization transfer saturation (MTsat), longitudinal relaxation (R1), transverse relaxation (R2*), isotropic volume fraction (ISOVF), intracellular volume fraction (ICVF), orientation dispersion (OD), fractional anisotropy*

(FA), mean diffusivity (MD), superficial white matter (SWM), deep white matter (DWM), periventricular white matter (PVWM), bootstrap ratio (BSR), systolic (SBP) and diastolic blood pressure (DBP), body mass index (BMI), waist-to-hip ratio (WHR), glycated hemoglobin (HbA1c), high-sensitivity C-reactive protein (CRP), hemoglobin, thyroid-stimulating hormone (TSH), free thyroxine (FT4).

Discussion

In this study in the community-dwelling population, we provided a detailed regionally-specific characterization of WMH and NAWM microstructure in aging-associated small vessel disease. Our analyses showed that WMHs are associated with reduced myelin-sensitive measures, decreased axonal metrics, and increased extracellular unbound water compartment markers as a function of distance from the lesion core. We also demonstrated that NAWM in individuals with WMH have regionally-specific pathology that correlates with the lesions volume. Finally, we provide significant evidence for the strong association between CVRs, their treatment and white matter microstructure. Together, these findings offer new insights into the detailed pattern of SVD-related damage and its systemic drivers in aging.

Damage extends beyond visible lesions

In line with the gradient model, our study provides compelling evidence that WMHs are not isolated lesions but markers of a broader pathological continuum, with distinct processes occurring at their core and periphery. While previous work brought evidence for centrifugal gradients of tissue damage (Maillard et al. 2014, 2011; Duering et al. 2013), we extend these findings by showing that lesion layers follow coherent age-sensitive patterns. WMH cores were characterised by age-independent loss of myelin and axons, suggesting irreversible damage. In contrast, outer layers displayed progressive, age-related demyelination and axonal rarefaction, pointing to an active front of degeneration. Extracellular water behaved differently, accumulating in both lesion cores and at intermediate distances, consistent with gliosis and extracellular matrix reorganization. Together, these findings refine the “WMH penumbra” model (Maillard et al. 2011; Voorter et al. 2024), showing that lesion centers, the areas captured by FLAIR imaging, represent an end-stage phenomenon, whereas the periphery remain dynamic, with age-sensitive zones of tissue vulnerability. This has direct implications for lesion tracking, as detection based on conventional MRI would likely underestimate the true extent of white matter pathology.

Cardiovascular drivers of microstructural damage

Our analysis links white matter microstructure not only to local lesion properties but also to systemic vascular and metabolic health. Lower NAWM myelin content, axonal disruption, and higher extracellular water were associated with older age, elevated systolic blood pressure (SBP), impaired glucose regulation (HbA1c), lower total and LDL cholesterol, and reduced hemoglobin. Medication patterns mirrored these relationships, with greater antihypertensive, antiplatelet, and anticoagulant use observed in individuals exhibiting the

same diffuse microstructural signature. These findings emphasize that white matter degeneration in aging is shaped as much by systemic health factors as by local lesion dynamics.

The negative association between LDL cholesterol and white matter microstructure may seem counterintuitive, given the traditional link between high cholesterol and poor health outcomes (Jung et al. 2022). However, cholesterol levels typically decline with age due to changes in diet, medication, and body composition (Johansson et al. 2012; Jousilahti et al. 1999; Matthews et al. 2009; Downer et al. 2014), and recent work has highlighted a 'cholesterol paradox,' where lower late-life cholesterol is associated with worse outcomes (S.-S. Wang et al. 2023; Ravnskov et al. 2016; Errigo et al. 2025). This interpretation is consistent with our finding that individuals with lower cholesterol and greater antihypertensive or antiplatelet use showed similar diffuse white matter pathology, likely reflecting higher vascular burden rather than direct treatment effects (Yoon et al. 2017; Xu et al. 2020; Zhu et al. 2020).

In line with established evidence, higher systolic blood pressure (Mok and Kim 2015) was strongly associated with microstructural damage, supporting the role of chronic hypertension in driving endothelial dysfunction, hypoperfusion, and blood–brain barrier disruption (C. E. Zhang et al. 2019; Li et al. 2017; Katsi et al. 2020). We also found that elevated HbA1c was linked to adverse white matter integrity, underscoring the contribution of chronic glucose dysregulation and metabolic dysfunction to diffuse tissue injury (D.-Q. Wang et al. 2020; Schweitzer et al. 2024; Weykamp 2013). Finally, low hemoglobin, which may signal reduced oxygen-carrying capacity and contribute to cerebral hypoxia, was similarly associated with vulnerability of the white matter ((Mairbäurl and Weber 2012; Inzitari et al. 2008). Together, these results highlight the combined influence of vascular, metabolic, and hematologic stressors in shaping cerebral small vessel disease pathology.

Microstructural fingerprints of WMH and NAWM

Our results challenge the notion of "normal" appearing white matter by demonstrating that NAWM exhibits subtle but significant microstructural pathology that scales with WMH volume. Specifically, reductions in myelin- and axon-sensitive metrics and increases in extracellular water indices in NAWM mirrored, albeit less severely, the characteristic profile seen within WMHs. This diffuse injury pattern is consistent with prior studies reporting NAWM abnormalities in individuals with WMH (Parent et al. 2025, 2023; Maniega et al. 2015; Bastin et al. 2009) and suggests that WMH burden serves as a surrogate marker of widespread tissue compromise rather than isolated focal lesions. Histopathological evidence supports these observations, showing that tissue beyond lesion borders may already harbor myelin rarefaction, axonal degeneration, and gliosis (Wardlaw, Valdés Hernández, and Muñoz-Maniega 2015). Together, these findings underscore the importance of moving beyond lesion-centric analyses: interventions and risk assessments should target the global white matter network, as NAWM pathology appears to represent a "pre-lesional" stage of small vessel disease with clinical relevance for aging and dementia risk. They also highlight

the added value of quantitative, non-FLAIR imaging, since FLAIR captures only the lesion cores and misses diffuse pathology in surrounding tissue.

Distinct regional patterns revealed by multivariate analysis

By combining multivariate analysis with regional stratification, we highlight anatomical vulnerabilities that shape how the WMH-related pathology propagates. The first principal component reflected a consistent pattern of myelin and axonal loss with elevated fluid-related metrics, clearly separating WMH from NAWM and peaking in periventricular regions. In contrast, the second component captured anatomical differences between SWM, DWM, and PVWM, largely driven by axonal orientation metrics, which may reflect either intrinsic tract organization or secondary axonal injury following myelin loss (Bullock et al. 2022). Importantly, greater lesion burden was associated with larger divergence between NAWM and WMH microstructure, particularly in periventricular frontal regions along the primary damage axis. In this region, NAWM microstructure was also most sensitive to the extent of lesion burden, underscoring that periventricular white matter is both a site of prominent lesion accumulation and a key region of diffuse tissue injury. Mechanistically, this vulnerability is explained by the location of PVWM within vascular watershed zones, where overlapping arterial territories predispose tissue to chronic hypoperfusion and reduced perfusion pressure (Torvik 1984; Kang et al. 2022; Kim, MacFall, and Payne 2008). By contrast, superficial white matter, especially in occipital and temporal lobes, showed minimal association between lesion burden and NAWM microstructure, suggesting relative resilience or distinct pathogenic pathways (Moody, Bell, and Challa 1990). These regional differences underscore the importance of considering vascular territories and microstructural context when interpreting WMH distribution and progression.

Community-based sampling reveals early, diffuse changes

A key strength of our study is the use of the BrainLaus dataset, a community-based cohort derived from the general population of Lausanne, Switzerland. This cohort provides critical insights into the asymptomatic stages of WMH development, which are particularly relevant for primary prevention strategies (de Leeuw et al. 2001). While a large number of WMH studies rely on clinical populations, which are highly valuable for understanding symptomatic or advanced disease, they are often subject to referral bias and may not reflect the broader aging population (Kokmen et al. 1996). In contrast, community-based samples offer greater generalizability but may be affected by healthy volunteer bias (Weuve et al. 2015; Brayne and Moffitt 2022). Integrating evidence from both study types is essential to fully capture the spectrum of WMH progression and the systemic mechanisms that drive it.

Limitations

Although our spatial and cross-sectional analyses suggest that WMH cores represent irreversible tissue loss and lesion edges dynamic zones of degeneration, these interpretations should be considered cautiously. WMHs can expand, stabilize, or regress over time (Wardlaw, Valdés Hernández, and Muñoz-Maniega 2015; Wardlaw, Smith, and Dichgans

2019; Promjunyakul et al. 2018) and our per-brain rather than per-lesion approach may obscure lesion-specific variability. Nevertheless, the consistency and effect sizes of our associations provide confidence that the observed gradients reflect dominant mechanisms of lesion evolution. Longitudinal and lesion-resolved studies are needed to validate whether the patterns we observe generalise across lesion trajectories.

Conclusions

Taken together, our findings redefine WMHs as visible endpoints of widespread white matter vulnerability shaped by systemic cardiovascular and metabolic stressors. By demonstrating coherent spatial gradients, diffuse NAWM pathology, regional vulnerabilities, and systemic drivers, we provide a framework that integrates whole-brain perspectives on aging-related small vessel disease. This highlights the importance of early and sustained vascular risk factor management, as well as the potential of advanced qMRI and dMRI to detect subtle changes that could inform prevention and intervention strategies in aging populations.

References

Andersson, Jesper L. R., and Stamatios N. Sotiropoulos. 2016. "An Integrated Approach to Correction for off-Resonance Effects and Subject Movement in Diffusion MR Imaging." *NeuroImage* 125 (January):1063–78.

Bastin, Mark E., Jonathan D. Clayden, Alison Pattie, Iona F. Gerrish, Joanna M. Wardlaw, and Ian J. Deary. 2009. "Diffusion Tensor and Magnetization Transfer MRI Measurements of Periventricular White Matter Hyperintensities in Old Age." *Neurobiology of Aging* 30 (1): 125–36.

Billot, Benjamin, Douglas N. Greve, Oula Puonti, Axel Thielscher, Koen Van Leemput, Bruce Fischl, Adrian V. Dalca, Juan Eugenio Iglesias, and ADNI. 2023. "SynthSeg: Segmentation of Brain MRI Scans of Any Contrast and Resolution without Retraining." *Medical Image Analysis* 86 (May):102789.

Brayne, Carol, and Terrie E. Moffitt. 2022. "The Limitations of Large-Scale Volunteer Databases to Address Inequalities and Global Challenges in Health and Aging." *Nature Aging* 2 (9): 775–83.

Bullock, Daniel N., Elena A. Hayday, Mark D. Grier, Wei Tang, Franco Pestilli, and Sarah R. Heilbronner. 2022. "A Taxonomy of the Brain's White Matter: Twenty-One Major Tracts for the 21st Century." *Cerebral Cortex (New York, N.Y.: 1991)* 32 (20): 4524–48.

Bussy, Aurélie, Jake P. Levy, Tristin Best, Raihaan Patel, Lani Cupo, Tim Van Langenhove, Jørgen E. Nielsen, et al. 2023. "Cerebellar and Subcortical Atrophy Contribute to Psychiatric Symptoms in Frontotemporal Dementia." *Human Brain Mapping* 44 (7): 2684–2700.

Bussy, Aurélie, Raihaan Patel, Olivier Parent, Alyssa Salaciak, Saashi A. Bedford, Sarah Farzin, Stephanie Tullo, et al. 2025. "Exploring Morphological and Microstructural Signatures across the Alzheimer's Spectrum and Risk Factors." *Neurobiology of Aging* 149 (May):1–18.

Bussy, Aurélie, Raihaan Patel, Eric Plitman, Stephanie Tullo, Alyssa Salaciak, Saashi A. Bedford, Sarah Farzin, et al. 2021. "Hippocampal Shape across the Healthy Lifespan

and Its Relationship with Cognition." *Neurobiology of Aging* 106 (October):153–68.
Callaghan, Martina F., Patrick Freund, Bogdan Draganski, Elaine Anderson, Marinella Cappelletti, Rumana Chowdhury, Joern Diedrichsen, et al. 2014. "Widespread Age-Related Differences in the Human Brain Microstructure Revealed by Quantitative Magnetic Resonance Imaging." *Neurobiology of Aging* 35 (8): 1862–72.
Cathala, Camille, Ferath Kherif, Jean-Philippe Thiran, Aurélie Bussy, and Bogdan Draganski. 2025. "WHITE-Net : White Matter HyperIntensities Tissue Extraction Using Deep Learning Network." *medRxiv*. https://doi.org/10.1101/2025.01.09.25320242.
Courtney, Michael, Daniel Carey, Stephen Murphy, Silvin Knight, James F. Meaney, Rose Anne Kenny, and Céline De Looze. 2025. "Connecting the Dots: Microstructural Properties of White Matter Hyperintensities Predict Longitudinal Cognitive Changes in Ageing." *Frontiers in Aging Neuroscience* 17 (February):1520069.
Daducci, Alessandro, Erick J. Canales-Rodríguez, Hui Zhang, Tim B. Dyrby, Daniel C. Alexander, and Jean-Philippe Thiran. 2015. "Accelerated Microstructure Imaging via Convex Optimization (AMICO) from Diffusion MRI Data." *NeuroImage* 105 (January):32–44.
Downer, Brian, Steven Estus, Yuriko Katsumata, and David W. Fardo. 2014. "Longitudinal Trajectories of Cholesterol from Midlife through Late Life according to Apolipoprotein E Allele Status." *International Journal of Environmental Research and Public Health* 11 (10): 10663–93.
Draganski, B., J. Ashburner, C. Hutton, F. Kherif, R. S. J. Frackowiak, G. Helms, and N. Weiskopf. 2011. "Regional Specificity of MRI Contrast Parameter Changes in Normal Ageing Revealed by Voxel-Based Quantification (VBQ)." *NeuroImage* 55 (4): 1423–34.
Duering, Marco, Endy Csanadi, Benno Gesierich, Eric Jouvent, Dominique Hervé, Stephan Seiler, Boubakeur Belaroussi, et al. 2013. "Incident Lacunes Preferentially Localize to the Edge of White Matter Hyperintensities: Insights into the Pathophysiology of Cerebral Small Vessel Disease." *Brain: A Journal of Neurology* 136 (Pt 9): 2717–26.
Errigo, Alessandra, Giovanni Mario Pes, Calogero Caruso, Giulia Accardi, Anna Aiello, Giuseppina Candore, and Sonya Vasto. 2025. "An Emerging Longevity Blue Zone in Sicily: The Case of Caltabellotta and the Sicani Mountains." *Preprints*. https://doi.org/10.20944/preprints202505.2113.v1.
Fazekas, F., J. B. Chawluk, A. Alavi, H. I. Hurtig, and R. A. Zimmerman. 1987. "MR Signal Abnormalities at 1.5 T in Alzheimer's Dementia and Normal Aging." *American Journal of Roentgenology* 149 (2): 351–56.
Firmann, Mathieu, Vladimir Mayor, Pedro Marques Vidal, Murielle Bochud, Alain Pécoud, Daniel Hayoz, Fred Paccaud, et al. 2008. "The CoLaus Study: A Population-Based Study to Investigate the Epidemiology and Genetic Determinants of Cardiovascular Risk Factors and Metabolic Syndrome." *BMC Cardiovascular Disorders* 8 (March):6.
Fukunaga, Masaki, Tie-Qiang Li, Peter van Gelderen, Jacco A. de Zwart, Karin Shmueli, Bing Yao, Jongho Lee, et al. 2010. "Layer-Specific Variation of Iron Content in Cerebral Cortex as a Source of MRI Contrast." *Proceedings of the National Academy of Sciences of the United States of America* 107 (8): 3834–39.
Grinberg, Lea Tenenholz, and Dietmar Rudolf Thal. 2010. "Vascular Pathology in the Aged Human Brain." *Acta Neuropathologica* 119 (3): 277–90.
Habes, Mohamad, Guray Erus, Jon B. Toledo, Tianhao Zhang, Nick Bryan, Lenore J. Launer, Yves Rosseel, et al. 2016. "White Matter Hyperintensities and Imaging Patterns of Brain Ageing in the General Population." *Brain: A Journal of Neurology* 139 (Pt 4): 1164–79.
Hajnal, J. V., D. J. Bryant, L. Kasuboski, P. M. Pattany, B. De Coene, P. D. Lewis, J. M. Pennock, A. Oatridge, I. R. Young, and G. M. Bydder. 1992. "Use of Fluid Attenuated Inversion Recovery (FLAIR) Pulse Sequences in MRI of the Brain." *Journal of*

Computer Assisted Tomography 16 (6): 841–44.
Helms, Gunther, Henning Dathe, and Peter Dechent. 2008. "Quantitative FLASH MRI at 3T Using a Rational Approximation of the Ernst Equation." *Magnetic Resonance in Medicine: Official Journal of the Society of Magnetic Resonance in Medicine / Society of Magnetic Resonance in Medicine* 59 (3): 667–72.
Hutton, Chloe, Andreas Bork, Oliver Josephs, Ralf Deichmann, John Ashburner, and Robert Turner. 2002. "Image Distortion Correction in fMRI: A Quantitative Evaluation." *NeuroImage* 16 (1): 217–40.
Inzitari, Marco, Stephanie Studenski, Caterina Rosano, Neil A. Zakai, William T. Longstreth Jr, Mary Cushman, and Anne B. Newman. 2008. "Anemia Is Associated with the Progression of White Matter Disease in Older Adults with High Blood Pressure: The Cardiovascular Health Study." *Journal of the American Geriatrics Society* 56 (10): 1867–72.
Iordanishvili, Elene, Melissa Schall, Ricardo Loução, Markus Zimmermann, Ketevan Kotetishvili, N. Jon Shah, and Ana-Maria Oros-Peusquens. 2019. "Quantitative MRI of Cerebral White Matter Hyperintensities: A New Approach towards Understanding the Underlying Pathology." *NeuroImage* 202 (116077): 116077.
Jenkinson, Mark, Peter Bannister, Michael Brady, and Stephen Smith. 2002. "Improved Optimization for the Robust and Accurate Linear Registration and Motion Correction of Brain Images." *NeuroImage* 17 (2): 825–41.
Jenkinson, M., and S. Smith. 2001. "A Global Optimisation Method for Robust Affine Registration of Brain Images." *Medical Image Analysis* 5 (2): 143–56.
Johansson, Ingegerd, Lena Maria Nilsson, Birgitta Stegmayr, Kurt Boman, Göran Hallmans, and Anna Winkvist. 2012. "Associations among 25-Year Trends in Diet, Cholesterol and BMI from 140,000 Observations in Men and Women in Northern Sweden." *Nutrition Journal* 11 (1): 40.
Jousilahti, P., E. Vartiainen, J. Tuomilehto, and P. Puska. 1999. "Sex, Age, Cardiovascular Risk Factors, and Coronary Heart Disease: A Prospective Follow-up Study of 14 786 Middle-Aged Men and Women in Finland." *Circulation* 99 (9): 1165–72.
Jung, Eujene, So Yeon Kong, Young Sun Ro, Hyun Ho Ryu, and Sang Do Shin. 2022. "Serum Cholesterol Levels and Risk of Cardiovascular Death: A Systematic Review and a Dose-Response Meta-Analysis of Prospective Cohort Studies." *International Journal of Environmental Research and Public Health* 19 (14): 8272.
Kang, Peter, Chunwei Ying, Yasheng Chen, Andria L. Ford, Hongyu An, and Jin-Moo Lee. 2022. "Oxygen Metabolic Stress and White Matter Injury in Patients with Cerebral Small Vessel Disease." *Stroke; a Journal of Cerebral Circulation* 53 (5): 1570–79.
Katsi, Vasiliki, Maria Marketou, Spyridon Maragkoudakis, Matthaios Didagelos, Georgios Charalambous, Fragkiskos Parthenakis, Costas Tsioufis, and Dimitrios Tousoulis. 2020. "Blood-Brain Barrier Dysfunction: The Undervalued Frontier of Hypertension." *Journal of Human Hypertension* 34 (10): 682–91.
Kim, Ki Woong, James R. MacFall, and Martha E. Payne. 2008. "Classification of White Matter Lesions on Magnetic Resonance Imaging in Elderly Persons." *Biological Psychiatry* 64 (4): 273–80.
Kokmen, E., Y. Ozsarfati, C. M. Beard, P. C. O'Brien, and W. A. Rocca. 1996. "Impact of Referral Bias on Clinical and Epidemiological Studies of Alzheimer's Disease." *Journal of Clinical Epidemiology* 49 (1): 79–83.
Lampe, Leonie, Rui Zhang, Frauke Beyer, Sebastian Huhn, Shahrzad Kharabian Masouleh, Sven Preusser, Pierre-Louis Bazin, Matthias L. Schroeter, Arno Villringer, and A. Veronica Witte. 2019. "Visceral Obesity Relates to Deep White Matter Hyperintensities via Inflammation." *Annals of Neurology* 85 (2): 194–203.

Leeuw, F. E. de, J. C. de Groot, E. Achten, M. Oudkerk, L. M. Ramos, R. Heijboer, A. Hofman, J. Jolles, J. van Gijn, and M. M. Breteler. 2001. "Prevalence of Cerebral White Matter Lesions in Elderly People: A Population Based Magnetic Resonance Imaging Study. The Rotterdam Scan Study." *Journal of Neurology, Neurosurgery, and Psychiatry* 70 (1): 9–14.

Li, Yue, Man Li, Xiaoyu Zhang, Qinglei Shi, Shuna Yang, Huimin Fan, Wei Qin, et al. 2017. "Higher Blood–brain Barrier Permeability Is Associated with Higher White Matter Hyperintensities Burden." *Journal of Neurology* 264 (7): 1474–81.

Lutti, Antoine, Frederic Dick, Martin I. Sereno, and Nikolaus Weiskopf. 2014. "Using High-Resolution Quantitative Mapping of R1 as an Index of Cortical Myelination." *NeuroImage* 93:176–88.

Lutti, Antoine, Chloe Hutton, Jürgen Finsterbusch, Gunther Helms, and Nikolaus Weiskopf. 2010. "Optimization and Validation of Methods for Mapping of the Radiofrequency Transmit Field at 3T." *Magnetic Resonance in Medicine: Official Journal of the Society of Magnetic Resonance in Medicine / Society of Magnetic Resonance in Medicine* 64 (1): 229–38.

Lutti, Antoine, Joerg Stadler, Oliver Josephs, Christian Windischberger, Oliver Speck, Johannes Bernarding, Chloe Hutton, and Nikolaus Weiskopf. 2012. "Robust and Fast Whole Brain Mapping of the RF Transmit Field B1 at 7T." *PloS One* 7 (3): e32379.

Maillard, Pauline, Evan Fletcher, Danielle Harvey, Owen Carmichael, Bruce Reed, Dan Mungas, and Charles DeCarli. 2011. "White Matter Hyperintensity Penumbra." *Stroke; a Journal of Cerebral Circulation* 42 (7): 1917–22.

Maillard, Pauline, Evan Fletcher, Samuel N. Lockhart, Alexandra E. Roach, Bruce Reed, Dan Mungas, Charles DeCarli, and Owen T. Carmichael. 2014. "White Matter Hyperintensities and Their Penumbra Lie along a Continuum of Injury in the Aging Brain." *Stroke; a Journal of Cerebral Circulation* 45 (6): 1721–26.

Mairbäurl, Heimo, and Roy E. Weber. 2012. "Oxygen Transport by Hemoglobin." *Comprehensive Physiology* 2 (2): 1463–89.

Maniega, Susana Muñoz, Maria C. Valdés Hernández, Jonathan D. Clayden, Natalie A. Royle, Catherine Murray, Zoe Morris, Benjamin S. Aribisala, et al. 2015. "White Matter Hyperintensities and Normal-Appearing White Matter Integrity in the Aging Brain." *Neurobiology of Aging* 36 (2): 909–18.

Manjón, José V., Pierrick Coupé, Luis Martí-Bonmatí, D. Louis Collins, and Montserrat Robles. 2010. "Adaptive Non-Local Means Denoising of MR Images with Spatially Varying Noise Levels." *Journal of Magnetic Resonance Imaging: JMRI* 31 (1): 192–203.

Matthews, Karen A., Sybil L. Crawford, Claudia U. Chae, Susan A. Everson-Rose, Mary Fran Sowers, Barbara Sternfeld, and Kim Sutton-Tyrrell. 2009. "Are Changes in Cardiovascular Disease Risk Factors in Midlife Women due to Chronological Aging or to the Menopausal Transition?" *Journal of the American College of Cardiology* 54 (25): 2366–73.

McIntosh, Anthony Randal, and Nancy J. Lobaugh. 2004. "Partial Least Squares Analysis of Neuroimaging Data: Applications and Advances." *NeuroImage* 23 Suppl 1:S250–63.

Mok, Vincent, and Jong S. Kim. 2015. "Prevention and Management of Cerebral Small Vessel Disease." *Journal of Stroke* 17 (2): 111–22.

Moody, D. M., M. A. Bell, and V. R. Challa. 1990. "Features of the Cerebral Vascular Pattern That Predict Vulnerability to Perfusion or Oxygenation Deficiency: An Anatomic Study." *AJNR. American Journal of Neuroradiology* 11 (3): 431–39.

Oliveira, Rita, Quentin Raynaud, Ileana Jelescu, Valerij G. Kiselev, Evgeniya Kirilina, and Antoine Lutti. 2025. "In Vivo Characterization of Magnetic Inclusions in the Subcortex

from Nonexponential Transverse Relaxation Decay." *NMR in Biomedicine* 38 (6): e70051.

Parent, Olivier, Zaki Alasmar, Sophia Osborne, Aurélie Bussy, Manuela Costantino, Jérémie P. Fouquet, Daniela Quesada, et al. 2025. "Characterizing Spatiotemporal White Matter Hyperintensity Pathophysiology in Vivo to Disentangle Vascular and Neurodegenerative Contributions." *medRxiv*. https://doi.org/10.1101/2025.06.10.25329342.

Parent, Olivier, Aurélie Bussy, Gabriel Allan Devenyi, Alyssa Dai, Manuela Costantino, Stephanie Tullo, Alyssa Salaciak, et al. 2023. "Assessment of White Matter Hyperintensity Severity Using Multimodal Magnetic Resonance Imaging." *Brain Communications* 5 (6): fcad279.

Patel, Raihaan, Christopher J. Steele, Anthony G. X. Chen, Sejal Patel, Gabriel A. Devenyi, Jürgen Germann, Christine L. Tardif, and M. Mallar Chakravarty. 2020. "Investigating Microstructural Variation in the Human Hippocampus Using Non-Negative Matrix Factorization." *NeuroImage* 207 (February):116348.

Penny, William D., Karl J. Friston, John T. Ashburner, Stefan J. Kiebel, and Thomas E. Nichols, eds. 2007. *Statistical Parametric Mapping: The Analysis of Functional Brain Images*. San Diego, CA: Academic Press.

Piguet, O., K. L. Double, J. J. Kril, J. Harasty, V. Macdonald, D. A. McRitchie, and G. M. Halliday. 2009. "White Matter Loss in Healthy Ageing: A Postmortem Analysis." *Neurobiology of Aging* 30 (8): 1288–95.

Preisig, Martin, Gérard Waeber, Peter Vollenweider, Pascal Bovet, Stéphane Rothen, Caroline Vandeleur, Patrice Guex, et al. 2009. "The PsyCoLaus Study: Methodology and Characteristics of the Sample of a Population-Based Survey on Psychiatric Disorders and Their Association with Genetic and Cardiovascular Risk Factors." *BMC Psychiatry* 9 (1): 1–12.

Promjunyakul, Nutta-On, Hiroko H. Dodge, David Lahna, Erin L. Boespflug, Jeffrey A. Kaye, William D. Rooney, and Lisa C. Silbert. 2018. "Baseline NAWM Structural Integrity and CBF Predict Periventricular WMH Expansion over Time." *Neurology* 90 (24): e2119–26.

Ravnskov, Uffe, David M. Diamond, Rokura Hama, Tomohito Hamazaki, Björn Hammarskjöld, Niamh Hynes, Malcolm Kendrick, et al. 2016. "Lack of an Association or an Inverse Association between Low-Density-Lipoprotein Cholesterol and Mortality in the Elderly: A Systematic Review." *BMJ Open* 6 (6): e010401.

Schilling, Sabrina, Christophe Tzourio, Carole Dufouil, Yicheng Zhu, Claudine Berr, Annick Alpérovitch, Fabrice Crivello, Bernard Mazoyer, and Stéphanie Debette. 2014. "Plasma Lipids and Cerebral Small Vessel Disease." *Neurology* 83 (20): 1844–52.

Schweitzer, Noah, Sang Joon Son, Howard Aizenstein, Shaolin Yang, Bistra Iordanova, Chang Hyung Hong, Hyun Woong Rho, et al. 2024. "Higher HbA1c Is Associated with Greater 2-Year Progression of White Matter Hyperintensities." *Diabetes* 73 (4): 604–10.

Sharma, Roopa, Sandeep Sekhon, Forshing Lui, and Marco Cascella. 2024. "White Matter Lesions." In *StatPearls*. Treasure Island (FL): StatPearls Publishing.

Slater, David A., Lester Melie-Garcia, Martin Preisig, Ferath Kherif, Antoine Lutti, and Bogdan Draganski. 2019. "Evolution of White Matter Tract Microstructure across the Life Span." *Human Brain Mapping* 40 (7): 2252–68.

Solé-Guardia, Gemma, Emma Custers, Arthur de Lange, Elyne Clijncke, Bram Geenen, Jose Gutierrez, Benno Küsters, et al. 2023. "Association between Hypertension and Neurovascular Inflammation in Both Normal-Appearing White Matter and White Matter Hyperintensities." *Acta Neuropathologica Communications* 11 (1): 2.

Stikov, Nikola, Jennifer S. W. Campbell, Thomas Stroh, Mariette Lavelée, Stephen Frey, Jennifer Novek, Stephen Nuara, et al. 2015. "In Vivo Histology of the Myelin G-Ratio

with Magnetic Resonance Imaging." *NeuroImage* 118 (September):397–405.
Stüber, Carsten, Markus Morawski, Andreas Schäfer, Christian Labadie, Miriam Wähnert, Christoph Leuze, Markus Streicher, et al. 2014. "Myelin and Iron Concentration in the Human Brain: A Quantitative Study of MRI Contrast." *NeuroImage* 93:95–106.
Tabelow, Karsten, Evelyne Balteau, John Ashburner, Martina F. Callaghan, Bogdan Draganski, Gunther Helms, Ferath Kherif, et al. 2019. "hMRI - A Toolbox for Quantitative MRI in Neuroscience and Clinical Research." *NeuroImage* 194 (July):191–210.
Tofts, Paul. 2003. *Quantitative MRI of the Brain: Measuring Changes Caused by Disease*. John Wiley & Sons.
Torvik, A. 1984. "The Pathogenesis of Watershed Infarcts in the Brain." *Stroke; a Journal of Cerebral Circulation* 15 (2): 221–23.
Tournier, J-Donald, Robert Smith, David Raffelt, Rami Tabbara, Thijs Dhollander, Maximilian Pietsch, Daan Christiaens, Ben Jeurissen, Chun-Hung Yeh, and Alan Connelly. 2019. "MRtrix3: A Fast, Flexible and Open Software Framework for Medical Image Processing and Visualisation." *NeuroImage* 202 (November):116137.
Veldsman, Michele, Petya Kindalova, Masud Husain, Ioannis Kosmidis, and Thomas E. Nichols. 2020. "Spatial Distribution and Cognitive Impact of Cerebrovascular Risk-Related White Matter Hyperintensities." *NeuroImage. Clinical* 28 (September):102405.
Voorter, Paulien H. M., Michael S. Stringer, Maud van Dinther, Daniëlle Kerkhofs, Anna Dewenter, Gordon W. Blair, Michael J. Thrippleton, et al. 2024. "Heterogeneity and Penumbra of White Matter Hyperintensities in Small Vessel Diseases Determined by Quantitative MRI." *Stroke; a Journal of Cerebral Circulation*, December. https://doi.org/10.1161/strokeaha.124.047910.
Wang, Dan-Qiong, Lei Wang, Miao-Miao Wei, Xiao-Shuang Xia, Xiao-Lin Tian, Xiao-Hong Cui, and Xin Li. 2020. "Relationship between Type 2 Diabetes and White Matter Hyperintensity: A Systematic Review." *Frontiers in Endocrinology* 11 (December):595962.
Wang, Sheng-Shu, Shan-Shan Yang, Chun-Jiang Pan, Jian-Hua Wang, Hao-Wei Li, Shi-Min Chen, Jun-Kai Hao, et al. 2023. "Cholesterol Paradox in the Community-Living Old Adults: Is Higher Better?" *Journal of Geriatric Cardiology: JGC* 20 (12): 837–44.
Wardlaw, Joanna M., Colin Smith, and Martin Dichgans. 2013. "Mechanisms of Sporadic Cerebral Small Vessel Disease: Insights from Neuroimaging." *Lancet Neurology* 12 (5): 483–97.
———. 2019. "Small Vessel Disease: Mechanisms and Clinical Implications." *Lancet Neurology* 18 (7): 684–96.
Wardlaw, Joanna M., Maria C. Valdés Hernández, and Susana Muñoz-Maniega. 2015. "What Are White Matter Hyperintensities Made of? Relevance to Vascular Cognitive Impairment." *Journal of the American Heart Association* 4 (6): 001140.
Wartolowska, Karolina Agnieszka, and Alastair John Stewart Webb. 2021. "Midlife Blood Pressure Is Associated with the Severity of White Matter Hyperintensities: Analysis of the UK Biobank Cohort Study." *European Heart Journal* 42 (7): 750–57.
Weiskopf, Nikolaus, Luke J. Edwards, Gunther Helms, Siawoosh Mohammadi, and Evgeniya Kirilina. 2021. "Quantitative Magnetic Resonance Imaging of Brain Anatomy and in Vivo Histology." *Nature Reviews. Physics* 3 (8): 570–88.
Weiskopf, Nikolaus, John Suckling, Guy Williams, Marta M. Correia, Becky Inkster, Roger Tait, Cinly Ooi, Edward T. Bullmore, and Antoine Lutti. 2013. "Quantitative Multi-Parameter Mapping of R1, PD(*), MT, and R2(*) at 3T: A Multi-Center Validation." *Frontiers in Neuroscience* 7 (June):95.

Weuve, Jennifer, Cécile Proust-Lima, Melinda C. Power, Alden L. Gross, Scott M. Hofer, Rodolphe Thiébaut, Geneviève Chêne, M. Maria Glymour, Carole Dufouil, and MELODEM Initiative. 2015. "Guidelines for Reporting Methodological Challenges and Evaluating Potential Bias in Dementia Research." *Alzheimer's & Dementia: The Journal of the Alzheimer's Association* 11 (9): 1098–1109.

Weykamp, Cas. 2013. "HbA1c: A Review of Analytical and Clinical Aspects." *Annals of Laboratory Medicine* 33 (6): 393–400.

Xu, Yu-Yuan, Li-Xia Zong, Chang-Qing Zhang, Yue-Song Pan, Jing Jing, Xia Meng, Hao Li, et al. 2020. "The Association of White Matter Hyperintensities with Stroke Outcomes and Antiplatelet Therapy in Minor Stroke Patients." *Annals of Translational Medicine* 8 (6): 331.

Yan, Yu, Yael Balbastre, Mikael Brudfors, and John Ashburner. 2021. "Factorisation-Based Image Labelling." *arXiv [cs.CV]*. arXiv. http://arxiv.org/abs/2111.10326.

Yoon, Cindy W., Yoonjae Choi, Seun Jeon, Dae Hyung Lee, Byung-Nam Yoon, Hee-Kwon Park, and Joung-Ho Rha. 2017. "Is Antiplatelet Treatment Effective at Attenuating the Progression of White Matter Hyperintensities?" *PloS One* 12 (4): e0176300.

Zeighami, Yashar, Seyed-Mohammad Fereshtehnejad, Mahsa Dadar, D. Louis Collins, Ronald B. Postuma, Bratislav Mišić, and Alain Dagher. 2019. "A Clinical-Anatomical Signature of Parkinson's Disease Identified with Partial Least Squares and Magnetic Resonance Imaging." *NeuroImage* 190 (April):69–78.

Zhang, C. Eleana, Sau May Wong, Renske Uiterwijk, Walter H. Backes, Jacobus F. A. Jansen, Cécile R. L. P. N. Jeukens, Robert J. van Oostenbrugge, and Julie Staals. 2019. "Blood-Brain Barrier Leakage in Relation to White Matter Hyperintensity Volume and Cognition in Small Vessel Disease and Normal Aging." *Brain Imaging and Behavior* 13 (2): 389–95.

Zhang, Hui, Torben Schneider, Claudia A. Wheeler-Kingshott, and Daniel C. Alexander. 2012. "NODDI: Practical in Vivo Neurite Orientation Dispersion and Density Imaging of the Human Brain." *NeuroImage* 61 (4): 1000–1016.

Zhu, Shiguang, Sifan Qian, Tan Xu, Hao Peng, Ruiguo Dong, Dunjing Wang, Xiaodong Yuan, et al. 2020. "White Matter Hyperintensity, Immediate Antihypertensive Treatment, and Functional Outcome after Acute Ischemic Stroke." *Stroke; a Journal of Cerebral Circulation* 51 (5): 1608–12.